Applied Physics Letters

Reliable material characterization at low x-ray energy through the phase-attenuation duality

Cite as: Appl. Phys. Lett. **120**, 124102 (2022); https://doi.org/10.1063/5.0085506
Submitted: 17 January 2022 • Accepted: 08 March 2022 • Published Online: 21 March 2022

Published open access through an agreement withPublished open access through an agreement with JISC Collections

I. Buchanan, A. Astolfo, M. Endrizzi, et al.

Applied Physics Letters ARTICLE scitation.org/journal/apl

Reliable material characterization at low x-ray energy through the phase-attenuation duality

Cite as: Appl. Phys. Lett. **120**, 124102 (2022); doi: 10.1063/5.0085506
Submitted: 17 January 2022 · Accepted: 8 March 2022 ·
Published Online: 21 March 2022

I. Buchanan,[1,a)] A. Astolfo,[1,2] M. Endrizzi,[1] D. Bate,[1,2] and A. Olivo[1]

AFFILIATIONS

[1]Department of Medical Physics and Biomedical Engineering, University College London, Gower Street, London WC1E 6BT, United Kingdom
[2]Nikon X-Tek Systems Ltd., Tring Business Centre, Tring, Hertfordshire, United Kingdom

[a)]Author to whom correspondence should be addressed: ian.buchanan.15@ucl.ac.uk

ABSTRACT

We present a comparison of between two polychromatic x-ray imaging techniques used to characterize materials: dual energy (DE) attenuation and phase-attenuation (PA), the latter being implemented via a scanning-based Edge Illumination system. The system-independent method to extract electron density and effective atomic number developed by Azevedo *et al.* IEEE Trans. Nucl. Sci. **63**, 341 (2016)—SIRZ—is employed for the analysis of planar images, with the same methodology being used for both approaches. We show PA to be more reliable at low energy x-ray spectra (40 kVp), where conventional DE breaks down due to insufficient separation of the energies used in measurements, and to produce results comparable with "standard" DE implemented at high energy (120 kVp), therefore, offering a valuable alternative in applications where the use of high x-ray energy is impractical.

With color x-ray imaging becoming increasingly popular thanks, in part, to a more widespread use of energy-discriminating detectors, a variety of methods have been proposed to enable material characterization (MC). This can be achieved via a general parameter space defined by physical quantities, such as Z effective (Z_{eff}) and electron density (ρ_e),[1–5] or by projecting measurements into specific material basis, such as bone and soft tissue.[6] In particular, DE is used extensively in security inspections,[7] medicine,[8] and some areas of material sciences.[9] In a polychromatic setting, DE requires a sufficiently broad spectrum in order to function reliably, as a significant contribution from the Compton effect is required to make low- and high-energy channels sufficiently independent.[10]

X-ray phase contrast imaging (XPCi) translates changes in the x-ray phase into detectable intensity differences. By considering the complex refractive index: $n = 1 - \delta(E) + i\beta(E)$, the real decrement from unity, δ, determines the overall phase shift $\Phi = k\int \delta(x, y, z; E)dz$, and $i\beta$ governs transmission $T = \exp(-2k\int \beta(x, y, z; E)dz)$, with k being the photon wavenumber and integration being over the photon's path through the sample. δ is proportional to electron density and is typically larger than β, meaning that small, weakly absorbing or thin samples are more visible in XPCi conditions than in conventional attenuation-based imaging. XPCi systems, such as Edge Illumination (EI) and Grating Interferometry (GI), have seen growing interest over the last few years, with much effort being made to translate these techniques into practical laboratory systems.[11]

Qi *et al.* showed that δ and β could be used in a manner equivalent to dual energy decomposition.[12] Contillo and Taibi developed this further by choosing a two-material basis into which (in their case, simulated) data were projected;[13] Braig *et al.* then provided experimental validation through CT data acquired with GI implemented on a compact synchrotron.[14] Subsequently, Mechlem *et al.* used simulated GI data to show that the simultaneous use of DE and PA holds promise for chest imaging,[6] and Schaff *et al.* used propagation-based XPCI to demonstrate that combining the phase retrieval and MC processes in a single step leads to significantly improved results.[15]

The present work directly compares laboratory-based PA and DE based MC with a single system. In particular, we show experimentally that PA MC outperforms DE MC at low spectral energies, where the latter breaks down due to the insufficient contribution from Compton scattering. We also present "gold-standard" DE measurements at 120 kVp and show that PA's MC capabilities at lower spectral energy are comparable to these. This has applications in areas where MC capabilities would be desirable, but the use of high-energy x rays is impossible or simply inconvenient.

Linear attenuation coefficient images are first obtained from transmission images via

$$\mu(E) = -\log(T(E))/t, \tag{1}$$

where t is the thickness of the sample. For MC, we begin with the Alvarez and Macovski decomposition of $\mu(E)$ into photoelectric and Compton components,[1] assuming that measurements are far from absorption edges

$$\mu(E) = (E^{-3})a_p + f_{KN}(E)a_c, \tag{2}$$

where a_p and a_c correspond to photoelectric and Compton contributions to attenuation, respectively, and $f_{KN}(E)$ is the Klein–Nishina formula.[16] In DE, $\mu(E)$ is decomposed into a_p and a_c by matrix division of Eq. (2), making use of multiple energy measurements of the transmission $T(E)$ and Eq. (1). a_c is directly proportional to the electron density[1] and, hence, to Φ

$$\rho_e = K_1 a_c, \tag{3a}$$

$$\rho_e = K_2 \Phi. \tag{3b}$$

K_1 and K_2 are coefficients that can be determined via calibration with reference materials. The theoretical expressions linking ρ_e to standard volumetric density (ρ) and δ[17,18] are

$$\rho_e = \sum_{i=1}^{N} \frac{Z_i}{R_i}\rho, \tag{4a}$$

$$\rho_e = \frac{k^2\delta(E)}{2\pi r_e A_n}, \tag{4b}$$

where Z_i is the atomic number of the ith element in the material, R_i is the areal electron density, r_e is the classical electron radius, and A_n is Avagadro's number. For both DE and PA methods, the electron density of a given material may, thus, be calculated as long as the sample thickness is known.

The effective atomic number, Z_e, is a non-integer atomic number whose elemental x-ray cross section matches that of a given material.[17] Theoretical values are calculated for reference materials, and experimental data can then be used to determine the unknown coefficients g and v in the model

$$Z_e = g\left(\frac{a_p}{a_c}\right)^{1/v}. \tag{5}$$

As stated above in the case of DE, a_p and a_c are determined by matrix division of Eq. (2), and the values are then used in Eq. (5) for MC. In PA, Eqs. (4b) and (5) are combined such that Z_e may be calculated in a single step

$$Z_e = gE^{3/v}\left[C\left(\frac{\mu(E)}{\Phi(E)}\right) - f_{KN}(E)\right]^{1/v}, \tag{6}$$

where $C = K_1/K_2$ is a constant. Note that the thickness t does not need to be known in order to calculate Z_e, as the ratio of different contrast channels is used in this calculation. In order to calculate the theoretical values of Z_e and ρ_e, it is necessary to know both the spectrum employed, and the characteristics of the materials used for calibration, i.e., their attenuation cross sections and refractive indices. The latter were obtained via the Xraylib software,[19] while the spectra for each kVp setting were generated using TASMICS[20] and corrected for the energy-dependent attenuation of the CdTe sensor layer used in the detector.

XPCi and attenuation measurements were taken using the laboratory x-ray system schematized in Fig. 1; the samples scanned are listed in Table I. A COMET MXR-160HP/11 x-ray source (Comet, Wünnewil-Flamatt, Switzerland) was used, and its effective focal spot reduced to 70 μm by means of an absorbing slit. Downstream, an Edge Illumination (EI) sample mask, M1, with period $p_{M_1} = 75\,\mu$m,

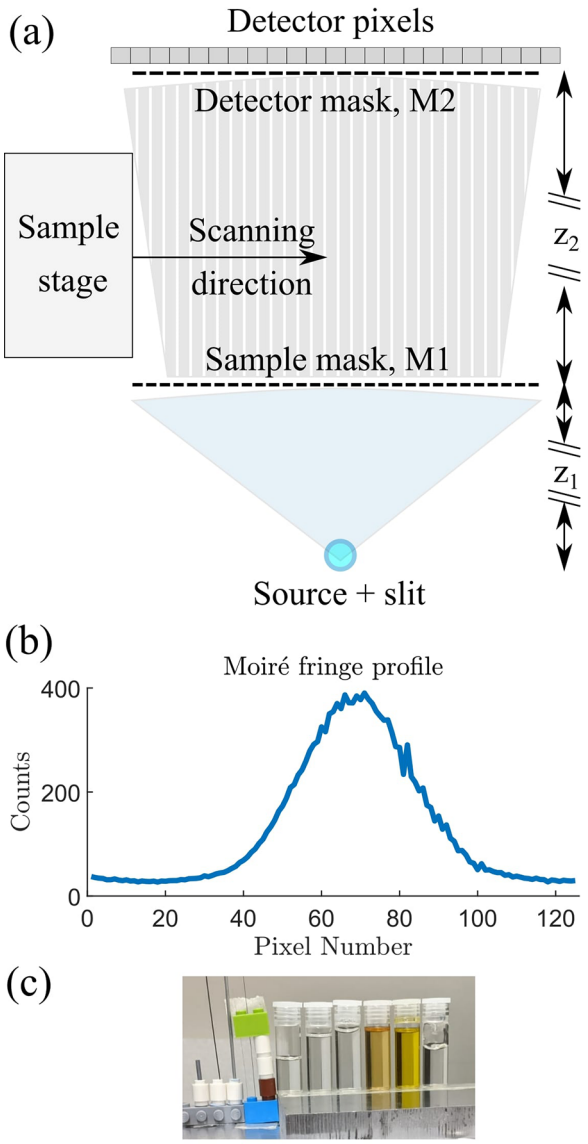

FIG. 1. (a) Moiré based scanning implementation of edge illumination. The projected pitch of M1 is slightly larger than that of M2, creating a Moiré fringe at the detector as shown in (b). Samples arranged on the sample stage—shown in (c)—are scanned across the field of view, with each pixel having a different sensitivity to changes in phase. From left to right, the samples are silicon, carbon, aluminum, sapphire, acetone, propan-2-ol, water, honey, olive oil, and hand gel.

TABLE I. Details of the (cylindrical) scanned samples. The shaded rows indicate that samples were obtained from Goodfellow Cambridge Ltd to ensure high purity for calibration.

Sample material	Radius/mm	Electron density/ moles cm^{-3}
Silicon	1	1.16
Aluminum	0.75	1.3
Carbon	0.25	1.13
Sapphire (Al_2O_3)	0.0625	1.95
Olive oil	5.53	NA
Acetone (C_3H_6O)	5.53	0.43
Propan-2-ol (C_3H_8O)	5.53	0.44
Honey	5.53	NA
Hand gel (water-alcohol mix)	5.53	NA
Water	5.53	0.55
Glass vial	6.37 (outer); 5.53 (inner)	NA

aperture sizes of 20.8 μm, and septa thicknesses of 300 μm split the beam into an array of beamlets. A detector mask M2 with the same septa thickness, period $p_{M_2} = 98\,\mu$m and aperture sizes of 28 μm, is placed immediately before the detector, blocking the edges of the 100 μm pixel edges. The detector is a dual energy, single photon counting CdTe-CMOS (XCounter) with 2048 vertical and 128 horizontal pixels.

M1 and M2 make the system sensitive to changes in the phase. Object-induced refraction, which is proportional to the first derivative of the phase, translates into a lateral shift of the beamlets at the detector. As a result, a different fraction of each beamlet is captured by the apertures in M2, and an increased or reduced intensity is measured. In the setup used for this experiment, the projected pitch of M1 was slightly greater than that of M2, resulting in a Moiré pattern across the detector, i.e., in each pixel column being illuminated to a slightly different degree. This is similar to the "asymmetric mask" implementation of EI[21] and to other fringe-based XPCi systems.[22] A sample is continuously scanned across the field of view immediately downstream of M1, with the detector acquiring images at regular intervals. The scan speed is set such that integer multiples or fractional periods of M1 are traversed during the acquisition of a single frame. The combination of images of the sample from each detector column allows for the application of phase retrieval algorithms: one period of the Moiré fringe is fitted to a normalized Gaussian plus offset for each row of the detector

$$\mathrm{fit}(a,b,c,d,x) = a\exp\left(\frac{-(x-b)^2}{2c}\right)\Big/\sqrt{2\pi c} + d, \qquad (7)$$

where c and d are required to be greater than zero and x is a vector whose limits are, by definition, $\pm p_{M_1}/2$, and contains the same number of elements as pixels used in the fit.

For each fitted row, frames containing the sample projected over the fringe are processed using a perturbation of Eq. (7) according to a minimization algorithm, i.e.,

$$\chi(t,r,s) = \arg\min\left\{\mathrm{fit}(a\,t,\ b - r\,z_2,\ c + s\,z_2^2,\ d\,t,\ x) - \mathrm{data}\right\}, \qquad (8)$$

where t is the object transmission, r is the refraction angle, and s is the ultra-small-angle-scattering distribution width in $\mu\mathrm{Rad}^2$. Transmission can be assumed to be the same for both Gaussian and offset because the masks are almost fully opaque for the x-ray spectra used here; hence, the offset intensity is due primarily to the finite source size.

The XCounter's low energy threshold (used to cut the noise) was set at 18.5 keV, and the middle threshold adjusted set such that the counts at the Moiré fringe peak were distributed approximately equally between low and high energy bins. For the PA measurements, samples placed immediately behind M1 were scanned continuously at a speed of one eighth of p_{M_1} per second, with frames acquired every second. Scans were repeated at 40 and 60 kVp tube voltages, and only the total energy bin was used in the analyses.

For the DE measurements, the samples were moved as close as possible to the detector in order to minimize phase effects. M1 was removed, but M2 was kept in place to ensure DE and PA were acquired at comparable resolutions (apart from the magnification factor); the scanning speed was also adjusted to compensate for the removal of M1. Voltages of 40, 60, and 120 kVp were used, with the data from the 60 kVp scans being made available in the supplementary material. The 128 horizontal detector pixels impose an upper limit of 128 images per scan. In practice, not all columns were used due to malfunctioning pixels or low flux near the detector edges.[23] In the DE case, images from individual columns are registered and combined in a weighted sum, with weights $w_i = \sqrt{N_i}$, where N_i is the number of background counts in each column. The final image is normalized to the background area; then, the samples are segmented and a line profile is extracted for each by averaging up to four pixel rows, with the exact number depending on the inclination of the sample with respect to the vertical. The linear attenuation coefficient, $\mu(E)$, is obtained as per Eq. (1) for both the high and low energy bins. Average values of $\mu(E_{low})$ and $\mu(E_{high})$ are extracted from the central area of the sample, where the signal is most stable.

In the PA setting, pixel columns within the central Moiré fringe are registered and processed using Eq. (7). The retrieved attenuation channel is processed in the same manner as described above to obtain values of $\mu(E)$. The refraction channel is directly proportional to the differential phase and must be integrated along the scanning direction to obtain the phase shift. The typical stripe artifacts associated with direct integration of refraction images were avoided by using the Fourier-space regularization algorithm developed by Massimi *et al.*[24] Images are then averaged to produce profiles, an example of which is shown in Fig. 2.

Also in this case, the thickness functions of each sample were used to obtain thickness-independent measurements of the phase shift, with an average value recorded from the central region where the signal was most stable.

Calibration materials were pre-selected as being silicon, aluminum, sapphire, water, acetone, and propan-2-ol, as these have known chemical compositions and densities. Sapphire was excluded when processing the low energy DE data as its small size and large refraction at these energies made it difficult to extract a reliable signal. Carbon was not included as a calibration material in any data set due to its high porosity and, hence, scattering signal, which made absorption measurements less reliable compared to the other, non-scattering materials. Signals for all liquids were adjusted by division (attenuation) and subtraction (phase) of the equivalent vial profiles.

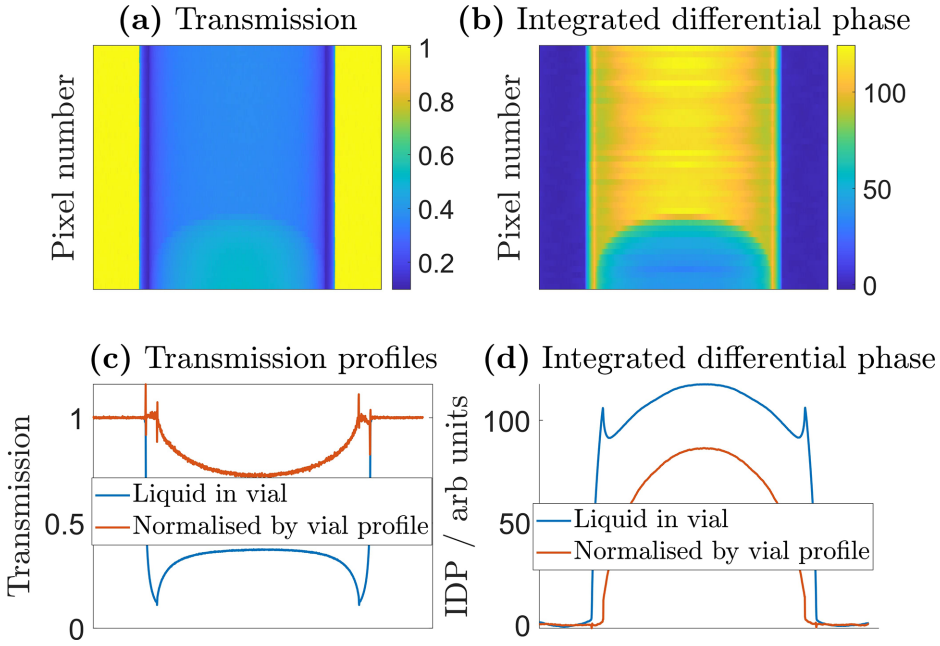

FIG. 2. Data normalization approach. Attenuation (a) and phase (b) images of acetone in a vial, with corresponding profiles before and after normalization by the vial profile in (c) and (d), respectively. Transmission normalization is achieved by dividing a profile taken from the liquid region by one from the vial-only region; the same applies to phase but uses subtraction rather than division. Normalization allows sample properties to be recovered independently from the container.

The forward model requires the average energy of attenuation measurements. Due to the vials' hardening of the x-ray beam, liquids were effectively being measured with a slightly higher energy x-ray spectrum than was used for the imaging of rods. To account for this, the measured $\mu(E)$ values of the calibration materials in-air and in-vials were used to look up appropriate values of E using Xraylib; the average energies, thus, obtained from the materials were then used in the analyses. In PA, the situation becomes more complicated due to the different effective energies associated with transmission and refraction measurements.[25] In EI, the effective energy of refraction measurements is greater than that of transmission in polychromatic settings. This means that the measured $\Phi(E)$ in Eq. (6) is associated with a greater energy than $\mu(E)$, i.e., that phase signals will be underestimated by some material and spectra-specific amount, and this underestimation will increase with energy. However, we can use the inferred energies from attenuation coefficients in our model and calculate the error that this produces in our phase measurements to show that it is negligible—see the supplementary material. The resulting energies used across the various settings are shown in Fig. 3.

The results of the material characterization algorithm for each method and kVp setting are shown in Fig. 4. In order to assess the performance of both methods, each of the high-purity materials' coordinates are linked to their theoretical values, calculated from simulated measurements which have been processed with same characterization algorithms as the experimental results.

The 40 kVp PA measurements show a good degree of material separation, with the hand gel (alcohol/water mixture) falling between water and the alcohols. Honey has a higher density than water and contains various sugar compounds: It falling between the water and carbon experimental measurements (in both methods) is also

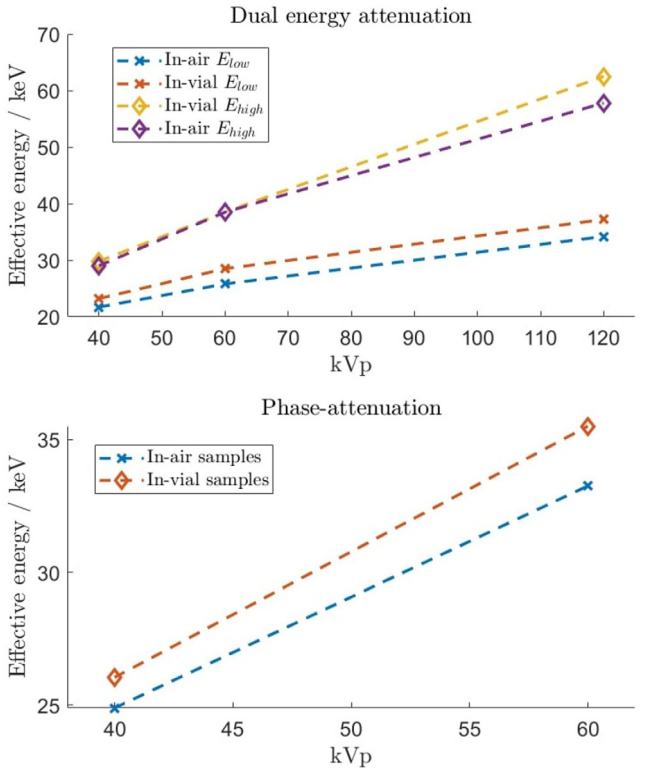

FIG. 3. Values of E used in the processing of data for both the DE method (a) and the PA method (b).

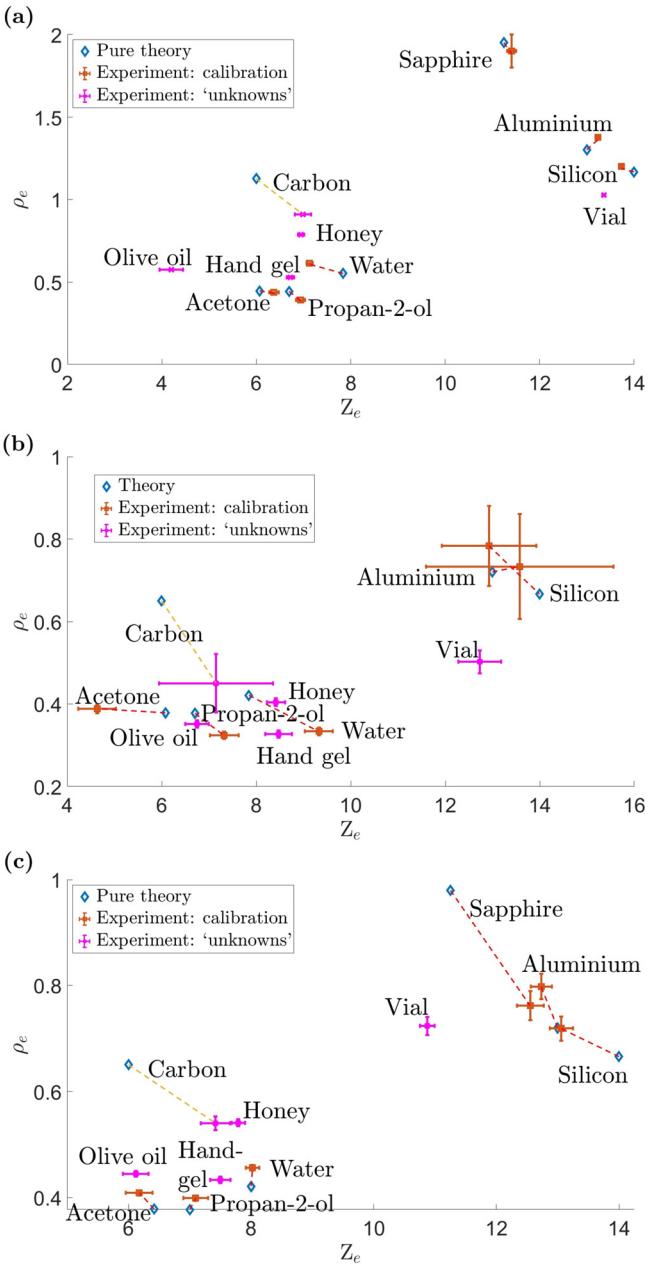

FIG. 4. Experimental results of the material characterization. Materials used to determine theoretical "target values," and by extension the calibration coefficients, are blue; the experimental counterparts are red. Where sample compositions are known, dashed lines join the theoretical values with experimental results. (a) shows the PA results for 40 kVp; (b) and (c) show the results for the DE approach using 40 and 120 kVp, respectively. Error bars correspond to the standard deviation of individual pixel values within a sample, as processed by the algorithm, relative to the mean result.

reasonable. That the experimental DE coordinate of honey is lower than the theoretical coordinate of water in the 40 kVp case is evidence of the DE method's unsuitability with lower average spectral energies. Olive oil is less dense that water but contains many hydrocarbon molecules similar to honey; both methods place it with a similar ρ_e and lower Z_e value than water. For the higher Z_e materials, the DE approach confuses aluminum and silicon, which appears to have a detrimental effect on the overall calibration, while the PA decomposition correctly places them close to the theoretical values. As said, sapphire was necessarily excluded from the low energy DE analysis, but PA succeeded in placing the material next to its theoretical coordinate. In order to have a quantitative quality metric, we have tabulated the average distance from experimental to theoretical coordinates by employing the simple formula

$$d_{Z_e} = \sqrt{\Sigma(Z_{e,experiment} - Z_{e,theory})^2}, \tag{9a}$$

$$d_{\rho_e} = \sqrt{\Sigma(\rho_{e,experiment} - \rho_{e,theory})^2}, \tag{9b}$$

and the results are shown in Table II.

The gold standard DE measurement, which makes use of wide ranging low and high energy bins, no longer confuses aluminum and silicon, though it does place the sapphire coordinate much closer to aluminum than any of the PA measurements. The lower Z_e materials are in this case also found to be in much better agreement with theory when compared with DE at 40 kVp. Carbon continues to be an outlier due to its high porosity causing a non-negligible amount of coherent scattering. The vial is a common borosilicate compound vial, whose SiO_2 content is expected to be roughly 75% of the total compound,[26] with the exact composition being unknown. The PA approach consistently places the vial close to the silicon coordinate, with slightly lower Z_e and ρ_e positions, while the DE method yields a less stable electron density coordinate and a notably lower Z_e value. We have compared the performance of material characterization (MC) via experimental x-ray measurements using both phase-attenuation (PA) and dual-energy (DE) decomposition methods for a variety of x-ray spectra. While computed tomography measurements are normally used in such characterization experiments, we used planar-only images to extract sample-specific measurements from an energy discriminating detector that separated photons into "low" and "high" energy bins. This lends itself to applications where objects have to be examined in a planar fashion, e.g., while on a conveyor belt, such as in security and some industrial inspection applications. The PA method shows greater accuracy and precision, particularly for the higher Z e materials, at lower energies, and compares favorably with the gold standard DE measurements acquired at a 120 kVp tube Voltage. A highly scattering carbon sample was inaccurately placed by both techniques for all energies considered, however, EI and other XPCi techniques that can quantify such scattering signals may be able to overcome this limitation in the future. In summary, we demonstrate that a PA implementation of this MC technique can overcome the known limitations

TABLE II. Average "distance" between projected experimental materials and the theoretical counterparts.

Setting	d_{Z_e}	d_{ρ_e}/moles cm^{-3}
40 kVp PA	0.9 ± 0.2	0.127 ± 0.002
40 kVp DE	2.5 ± 0.9	0.39 ± 0.04
120 kVp DE	1.7 ± 0.7	0.6 ± 0.1

encountered by DE at low spectral energies and can, therefore, be used as a valuable replacement where the use of low-energy x rays is preferable or necessary. A low-energy implementation of a reliable MC method allows reducing shielding requirements and, therefore, realizing cheaper and lighter scanners for security applications, such as the identification of liquids and the scanning of small postal packages, as well as for, e.g., the imaging of biomedical samples or low-Z industrial components.

See the supplementary material that contains additional experimental results comparing PA and DE using a 60 kVp beam and an analysis of the error caused by effective energies for phase and attenuation measurements being different.

This project was partially funded under the Innovative Research Call in Explosives and Weapons Detection. This is a Cross-Government programme sponsored by a number of Departments and Agencies under the UK Government's CONTEST strategy, in partnership with the U.S. Department of Homeland Security, Science and Technology Directorate. The views expressed in this publication are those of the authors and not necessarily those of funding contributors. AO is supported by the Royal Academy of Engineering under their Chairs in Emerging Technologies scheme. Additional support was obtained from the EPSRC (Grant No. EP/T005408/1).

AUTHOR DECLARATIONS

Conflict of Interest

The authors have no conflicts to disclose.

DATA AVAILABILITY

The data that support the findings of this study are available from the corresponding author upon reasonable request.

REFERENCES

[1]R. E. Alvarez and A. Macovski, "Energy-selective reconstructions in x-ray computerised tomography," Phys. Med. Biol. **21**, 733–744 (1976).
[2]L. A. Lehmann, R. E. Alvarez, A. Macovski, W. R. Brody, N. J. Pelc, S. J. Riederer, and A. L. Hall, "Generalized image combinations in dual KVP digital radiography," Med. Phys. **8**, 659–667 (1981).
[3]Z. Ying, R. Naidu, and C. Crawford, "Dual energy computed tomography for explosive detection," J. X-Ray Sci. Technol. **14**, 235–256 (2006).
[4]V. Rebuffel and J-M Dinten, "Dual-energy x-ray imaging: Benefits and limits," Insight **49**, 589–594 (2007).
[5]A. C. Silva, B. G. Morse, A. K. Hara, R. G. Paden, N. Hongo, and W. Pavlicek, "Dual-energy (spectral) CT: Applications in abdominal imaging," RadioGraphics **31**, 1031–1046 (2011).
[6]K. Mechlem, T. Sellerer, M. Viermetz, J. Herzen, and F. Pfeiffer, "Spectral differential phase contrast x-ray radiography," IEEE Trans. Med. Imaging **39**, 578–587 (2020).
[7]G. Chen, G. Bennett, and D. Perticone, "Dual-energy x-ray radiography for automatic high-z material detection," Nucl. Instrum. Methods Phys. Res., Sect. B **261**, 356–359 (2007).
[8]J.-M. Dinten, C. Robert-Coutant, and M. Darboux, "Dual-energy x-ray absorptiometry using 2D digital radiography detector: Application to bone densitometry," Proc. SPIE **4320**, 459–468 (2001).
[9]J. Letang, N. Freud, and G. Peix, "Signal-to-noise ratio criterion for the optimization of dual-energy acquisition using virtual x-ray imaging: Application to glass wool," J. Electron. Imaging **13**, 436–449 (2004).
[10]P. Vock and Z. Szucs-Farkas, "Dual energy subtraction: Principles and clinical applications," Eur. J. Radiol. **72**, 231–237 (2009).
[11]A. Olivo, "Edge-illumination x-ray phase-contrast imaging," J. Phys.: Condens. Matter **33**, 363002 (2021).
[12]Z. Qi, J. Zambelli, N. Bevins, and G.-H. Chen, "Quantitative imaging of electron density and effective atomic number using phase contrast CT," Phys. Med. Biol. **55**, 2669–2677 (2010).
[13]A. Contillo and A. Taibi, "Material characterisation in phase contrast imaging: The basis decomposition method revisited," Europhys. Lett. **117**, 48003 (2017).
[14]E. Braig, J. Böhm, M. Dierolf, C. Jud, B. Günther, K. Mechlem, S. Allner, T. Sellerer, K. Achterhold, B. Gleich, P. Noël, D. Pfeiffer, E. Rummeny, J. Herzen, and F. Pfeiffer, "Direct quantitative material decomposition employing grating-based x-ray phase-contrast CT," Sci. Rep. **8**, 16394 (2018).
[15]F. Schaff, K. S. Morgan, J. A. Pollock, L. C. P. Croton, S. B. Hooper, and M. J. Kitchen, "Material decomposition using spectral propagation-based phase-contrast x-ray imaging," IEEE Trans. Med. Imaging **39**, 3891–3899 (2020).
[16]O. Klein and Y. Nishina, "Über die streuung von strahlung durch freie elektronen nach der neuen relativistischen quantendynamik von Dirac," Z. Phys. **52**, 853–868 (1929).
[17]S. Azevedo, H. Martz, M. Aufderheide, W. Brown, K. Champley, J. Kallman, G. Roberson, D. Schneberk, I. Seetho, and J. Smith, "System-independent characterization of materials using dual-energy computed tomography," IEEE Trans. Nucl. Sci. **63**, 341–350 (2016).
[18]D. Paganin, *Coherent X-Ray Optics* (Oxford University Press, 2006), pp. 108–114.
[19]T. Schoonjans, A. Brunetti, B. Golosio, M. Sanchez del Rio, V. A. Solé, C. Ferrero, and L. Vincze, "The xraylib library for x-ray–matter interactions. Recent developments," Spectrochim. Acta, Part B **66**, 776–784 (2011).
[20]A. M. Hernandez and J. M. Boone, "Tungsten anode spectral model using interpolating cubic splines: Unfiltered x-ray spectra from 20 kv to 640 kv," Med. Phys. **41**, 042101 (2014).
[21]M. Endrizzi, A. Astolfo, F. A. Vittoria, T. P. Millard, and A. Olivo, "Asymmetric masks for laboratory-based x-ray phase-contrast imaging with edge illumination," Sci. Rep. **6**, 25466 (2016).
[22]H. Miao, A. Panna, A. A. Gomella, E. E. Bennett, S. Znati, L. Chen, and H. Wen, "A universal moiré effect and application in x-ray phase-contrast imaging," Nat. Phys. **12**, 830–834 (2016). pMC5063246[pmcid].
[23]I. Buchanan, G. Kallon, T. Beckenbach, J. Schulz, M. Endrizzi, and A. Olivo, "Effective modeling of high-energy laboratory-based x-ray phase contrast imaging utilizing absorption masks or gratings," J. Appl. Phys. **128**, 214503 (2020).
[24]L. Massimi, I. Buchanan, A. Astolfo, M. Endrizzi, and A. Olivo, "Fast, non-iterative algorithm for quantitative integration of x-ray differential phase-contrast images," Opt. Express **28**, 39677–39687 (2020).
[25]P. R. T. Munro and A. Olivo, "X-ray phase-contrast imaging with polychromatic sources and the concept of effective energy," Phys. Rev. A **87**, 053838 (2013).
[26]Y. Yue, M. I. Tuheen, and J. Du, "Borosilicate glasses," in *Encyclopedia of Materials: Technical Ceramics and Glasses*, edited by M. Pomeroy (Elsevier, Oxford, 2021), pp. 519–539.